Volume 1 | Number 1 | Jan 2013 | Pages 1–100

Journal of
Materials Chemistry A

Materials for energy and sustainability
www.rsc.org/materialsA

Li⁺

ROYAL SOCIETY
OF CHEMISTRY

ROYAL SOCIETY
OF CHEMISTRY

www.rsc.org/materialsA

1　**FeN Stabilized FeN@Pt Core-Shell Nanostructures for Oxygen Reduction**

2　**Reaction**

3

4　Xiao Ding[1,2], Shibin Yin[1,2,3*], Kang An[1,2], Lin Luo[2,3], Nai Shi[1], Yinghuai Qiang[1],

5　Sivakumar Pasupathi[3], Bruno G. Pollet[3], Pei Kang Shen[4*]

6　[1] School of Materials Science and Engineering, China University of Mining and

7　Technology, Xuzhou 221116, Jiangsu, China

8　[2] Low Carbon Energy Institute, China University of Mining and Technology, Xuzhou

9　221116, Jiangsu, China

10　[3] South African Institute for Advanced Materials Chemistry (SAIAMC), University of

11　the Western Cape, Private Bag X17, Bellville 7535, Cape Town, South Africa

12　[4] Collaborative Innovation Center of Sustainable Energy Materials, Guangxi

13　University, Nanning, 530004, China

14　* Corresponding authors. Tel.: +86-516-83883501; fax: +86-516-83883501. E-mail:

15　shibinyin@126.com (S.B. Yin);

16　Tel.: +86-771-3270152; fax: +86-771-3270152. E-mail: pkshen@gxu.edu.cn (P.K.

17　Shen).

18　**Abstract**

19　　The high cost and poor stability of catalysts are the main obstacles for the

20　commercialization of proton exchange membrane (PEM) fuel cells, especially, the

21　catalysts for oxygen reduction reaction (ORR). Here, the PtFe nanocatalysts with

22　different Pt to Fe atomic ratios are prepared by the impregnation-reduction method

23　and subsequently thermal annealing in NH_3 at ambient pressure. The XRD, STEM,

24　XPS and ICP are employed to investigate the corresponding physico-chemical

25　properties of the as-prepared catalysts, which demonstrate that the samples are Pt-rich

26　core-shell nanostructures. The cyclic voltammetry method is used to investigate their

27　electrochemical performance and the results show that these catalysts display high

28　ORR activity in O_2-saturated 0.1 mol L^{-1} $HClO_4$ aqueous solutions, $PtFe_3N/C$

29　displaying the highest mass activity of 369.32 mA mg^{-1} Pt in 0.90 V *vs*. RHE, which

30　is about 3 times higher than that of the commercial Pt/C (129.15 mA mg^{-1} Pt) at the

31 same potential. Moreover, it is also found that the as-prepared catalysts are almost 2

32 times more stable than the commercial Pt/C. The ORR activity is slightly affected

33 after 30,000 cycles in O_2-saturated $HClO_4$ aqueous solutions. This low cost ORR

34 catalyst exhibiting high performance opens up possibilities for designing core-shell

35 nanostructures for energy conversion.

1. Introduction

37 Proton exchange membrane (PEM) fuel cells have advantages in high efficiency

38 and low environmental benignity for hydrogen and oxygen conversion, but their

39 commercialization is hindered by the high cost and poor stability of the catalysts.

40 Especially, the catalysts for the oxygen reduction reaction (ORR) are critical for PEM

41 fuel cells[1,2] due to the sluggish oxygen reduction reaction at the cathode side.

42 Although fruitful achievements have been achieved,[3-9] further reduction through the

43 development of more active and stable catalysts is still required and a challenge.

44 It was observed that Pt alloys, such as PtFe,[10] PtCo[11] and PtNi,[12,13] exhibit good

45 ORR activities in acidic solutions, due to the lattice parameter strain effect[14] and

46 surface electron ligand effect[15] that decrease the Pt-Pt distance which in turns reduce

47 the activation energy and improve the ORR performance. While, these alloys cannot

48 prohibit the Fe, Co, Ni dissolved in acidic solutions, especially the acid-dissolvable

49 metal of Fe, which is harmful to the membrane and catalyst layer and influence their

50 stability.[16]

51 Core-shell catalysts that usually using Pt or Pd as shell, and other transition metals

52 as core, which could efficiently prevent these acid-dissolvable metals dissolving in

53 acidic solutions.[17-19] Recent efforts have been devoted toward the optimization and

54 design of core-shell catalysts with minimum use of Pt by adopting the galvanic

55 displacement,[20] spontaneous displacement reaction,[17, 21] and dealloying method.[22,23]

56 These methods could improve the catalytic performance, although large-scale

57 synthesis of core-shell catalysts with good stability still remains a challenge.[24,25]

58 According to the results reported by Kuttiyiel et al., the core in the core-shell catalysts

59 plays an important role to support the shell and improve the corresponding stability by

60   enhancing the chemical interactions between the core and the shell.[26] Meanwhile, as

61   reported by Gan *et al*., the compressive strain formed in the Pt shell surrounding the

62   Pt alloy core with a relatively smaller lattice parameter plays a dominant role in their

63   high ORR activities.[14] This means that the ORR activities could be experimentally

64   controlled by the lattice strain effect, which could be achieved by controlling the Pt

65   shell thickness and the alloy core composition. From this point of view, the

66   composition of the catalysts is considered to be one of the most important factors that

67   determine the catalytic activity for ORR.[27] Herein, we report the structure and the

68   performance of a core-shell nanoparticle consisting of a Pt shell on a FeN core. The

69   PtFeN nanocatalysts with different Pt to Fe atomic ratios were prepared by the

70   impregnation-reduction method and subsequently thermal annealing in NH_3 at

71   ambient pressure. The corresponding physico-chemical characterizations prove that

72   the as-prepared catalysts are of core-shell structures. Meanwhile, it also demonstrates

73   intriguing properties, which are much more active than the commercial Pt/C (40 wt%

74   Pt, Johnson Matthey) catalysts. Moreover, it was found that the ORR activity was

75   slightly affected after 30,000 cycles in O_2-saturated perchloric acid solutions, which

76   clearly demonstrates that the as-prepared catalysts are much more stable than the

77   commercial Pt/C.

78   **2. Experimental**

79   *2.1 Catalysts preparation*

80   The catalysts with metal loadings of 20 wt% and atomic ratios of Pt to Fe varying

81   from 1:1 to 1:5 were synthesized by the impregnation-reduction method, followed by

82   a high-temperature post treatment and dealloyed by chemical leaching as follows.

83   Firstly, given amounts of $H_2PtCl_6 \cdot 6H_2O$ and $FeCl_3 \cdot 6H_2O$ as starting precursors were

84   well mixed with deionized water in an ultrasonic bath, and then, the Vulcan XC-72 as

85   carbon support was added into the mixture. The well-dispersed slurry was obtained

86   with stirring and ultrasonication for 15 min, and then reduced by $NaBH_4$. After

87   impregnation for several hours, the color turned from yellow to colorless, the resulting

88   black solid samples were filtrated, washed and dried at 80 ^{o}C for 12 h in a vacuum

89   oven. Secondly, after grinding, the resulting dark powder was heated in a tube furnace

90   at 350 °C under flowing of H_2/Ar (5% H_2) for 1 h and followed by annealing at

91   650 °C under flowing of NH_3 for 2 h at heating rate of 10 °C min^{-1}. After cooling

92   down to room temperature, the powders were thoroughly washed in 0.1 mol L^{-1}

93   H_2SO_4 aqueous solutions for several hours to remove parts of Fe that on the surface.

94   Then, the samples were filtrated, washed and dried at 80 °C for 12 h in a vacuum oven.

95   The obtained samples were denoted as PtFeN/C, $PtFe_3N/C$ and $PtFe_5N/C$, respectively.

96   Moreover, the FeN/C was also prepared by the impregnation-reduction method and

97   followed by a high-temperature post treatment, but without the acid wash step.

98   *2.2 Catalysts characterization*

99   X-ray powder diffraction (XRD) measurements were carried out on a D8 advance

100   X-ray diffractometer (BRUKER AXS, Germany), using Cu *Ka* radiation ($\lambda = 0.15406$

101   nm), and operating at 40 kV and 30 mA. The 2θ angular regions between 20° and 90°

102   were finely scanned at 5° min^{-1} to obtain the crystal size and lattice parameter

103   according to the Scherrer equation and Vegard's law.[28] Scanning transmission electron

104   microscopy (STEM) and energy dispersive X-ray spectroscopy (EDX) measurements

105   were carried out in F-30 at 200 kV to obtain information of structure and particle size

106   distribution of the as-prepared catalysts. High-resolution STEM and electron

107   energy-loss spectroscopy (EELS) mapping were performed using a FEI TITAN

108   80-300 electron microscope (300 kV) equipped with a probe corrector (CEOS) and a

109   high-angle annular dark field (HAADF) detector. The Pt and Fe contents were

110   quantified by inductively coupled plasma atomic emission spectroscopy (ICP-AES,

111   PerkinElmer, Germany). X-ray photoelectron spectroscopy (XPS) measurements were

112   obtained by using a ESCALAB 250 Xi (Thermo Fisher Scientific, USA) with the Al

113   X-ray source operated at 150 W. Survey spectra were collected at pass energy (PE) of

114   100.0 eV over the binding energy range 0–1350 eV.

115   All electrochemical measurements were conducted using a bipotentiostat WD-20

116   BASIC (Pine Research Instrumentation, USA) in a thermostatically-controlled

117   standard three-electrode cell at 25 °C, adopting a platinum foil and Ag/AgCl as

118   counter electrode and reference electrode, respectively. The Ag/AgCl was calibrated

4

119   against a reversible hydrogen electrode (RHE) as reported.[29] A rotating disk electrode

120   (RDE) with a diameter of 5.0 mm was used as the substrate for the catalysts thin film

121   in the electrochemical measurements. The thin film catalysts layer was prepared as the

122   working electrode as follows. A mixture containing 10.0 mg catalysts, 960 μL ethanol

123   and 40 μL Nafion® solution (5.0 wt%) were dispersed in a ultrasonic bath for 15 min

124   to obtain a well-dispersed ink. The ink was then quantitatively transferred onto the

125   surface of glass carbon electrode using a micropipette, and dried under an infrared

126   lamp to obtain a catalyst thin film. The estimated catalysts loading were 0.51 mg cm^{-2}

127   for the as-prepared catalysts and 0.20 mg cm^{-2} for commercial Pt/C catalysts in this

128   study. Cyclic voltammetry (CV) experiments were carried out in N_2-saturated 0.1 mol

129   L^{-1} HClO$_4$ aqueous solutions with the scan rate of 50 mV s^{-1}. The accelerated

130   durability tests (ADT) were conducted by the CV method between 0 to 1.1 V *vs*. RHE

131   in O_2-saturated 0.1 mol L^{-1} HClO$_4$ aqueous solutions. For the oxygen reduction

132   experiment, the test was carried out in an O_2-saturated 0.1 mol L^{-1} HClO$_4$ aqueous

133   solutions scanned from 0 to 1.1 V *vs*. RHE at a rotating speed of 1600 rpm with a scan

134   rate of 5 mV s^{-1}. The background current was also measured by running a CV in

135   N_2-saturated 0.1 mol L^{-1} HClO$_4$ aqueous solutions scanned from 0 to 1.1 V *vs*. RHE

136   at a rotating speed of 1600 rpm with a scan rate of 5 mV s^{-1} either before or after the

137   ORR measurement to account for the capacitive current contributions. This

138   background current was subtracted from the experimental ORR current to eliminate

139   any capacitive current contributions. The ORR activity with *iR correction* corrected, it

140   was found that the uncompensated ohmic electrolyte resistance was about 20 Ω

141   measured *via* high frequency ac impedance in O_2-saturated 0.1 mol L^{-1} HClO$_4$

142   aqueous solutions. This value is in good agreement with those reported in the

143   literature for similar electrolytes.[30] The potentials were *iR* corrected by using the

144   following equation:

145        $E_{iR\text{-}correction}=E_{applied}-iR$ (1)

146   where *i* is the ORR measured current and *R* is the uncompensated ohmic electrolyte

147   resistance.

148 **3. Results and discussion**

149   As shown in Figure 1(a), XRD patterns for all the Pt and Fe in as-prepared catalysts

150 exhibit the typical characteristics of a crystalline face centered cubic (fcc) structure.

151 The 2θ of 23.09^{o} (100), 41.14^{o} (111), 47.19^{o} (200), 68.95^{o} (220), 70.56^{o} (202), and

152 83.55^{o} (311) are indicating the characteristic diffraction peaks of polycrystalline PtFe

153 (PDF#65-1051). The 2θ of 39.76^{o} (111), 46.243^{o} (200), 67.45^{o} (220) and 81.29^{o} (311)

154 are indicating the characteristic diffraction peaks of polycrystalline Pt (PDF#04-0802).

155 The 2θ of 23.45^{o} (100), 33.36^{o} (110), 41.17^{o} (111), 47.91^{o} (200), 70.06^{o} (220) and

156 84.65^{o} (311) are indicating the characteristic diffraction peaks of Fe_4N (PDF#06-0627).

157 The 2θ of 43.43^{o} (111) and 57.05^{o} (112) are indicating the characteristic diffraction

158 peaks of Fe_3N (PDF#49-1662). Obviously, the core is made of Fe_4N and Fe_3N.

159   The (111) peaks were fitted to a Gaussian line shape, as displayed in Figure 1(b), so

160 that the position of the peaks maximum (θ_{max}) and the full-width at half-maximum

161 ($B_{2\theta}$) can be obtained precisely.

162   The lattice parameters of the Pt fcc crystallites, a, were calculated from θ_{max}

163 according to the Vegard's law:[28]

164
$$a = \frac{\sqrt{2}\lambda_{k\alpha1}}{\sin\theta_{max}} \tag{2}$$

165 where $\lambda_{k\alpha1} = 0.154056$ nm. The lattice parameters of the Pt fcc crystallite in PtFeN/C,

166 PtFe$_3$N/C, and PtFe$_5$N/C that calculated according to Vegard's rule were 6.2336 Å,

167 6.2725 Å, and 6.2517 Å, while this value for FeN/C and commercial Pt/C were

168 6.2063 Å and 6.4106 Å. The differences in the lattice parameters could be attributed

169 to the incorporation of Fe atoms into Pt lattice to form a PtFe alloy in the as-prepared

170 catalysts. Compared with Pt/C, the lattice parameters of PtFeN/C, PtFe$_3$N/C and

171 PtFe$_5$N/C been compressed 0.1770 Å, 0.1381 Å and 0.1588 Å, in the sequence of

172 PtFeN/C > PtFe$_5$N/C > PtFe$_3$N/C. This finding indicates that the different Fe contents

173 could modify the surface state of the as-prepared catalysts, which is in very good

174 agreement with previous reports.[14] The average crystalline sizes of PtFeN/C,

175 PtFe$_3$N/C, PtFe$_5$N/C, FeN/C and Pt/C were calculated using the Scherrer equation and

176   were found to be 14.73 nm, 9.72 nm, 10.13 nm, 12.51 nm and 2.71 nm, respectively.

177   The corresponding results of the XRD analyses of the as-prepared catalysts are

178   summarized in Table 1.

179   Figure 2(a, b) display a pair of overview STEM images of PtFe$_3$N/C nanoparticles

180   after acidic dealloying. The images show that a majority of the particles are well

181   dispersed on the carbon support and with average particle sizes of about 6.8 nm in

182   diameter. Meanwhile, the EDX and EELS mapping are invaluable tools for

183   elucidating the composition and morphology of bimetallic nanoparticles. Figure 2(c)

184   shows the EDX mapping of a PtFe$_3$N/C nanoparticle after acidic dealloying, which

185   may prove the co-existence of Pt and Fe. While, the N is negligible and also

186   overlapped with C, this may be attributed to the relatively low reduction temperature

187   and the doping effect of NH$_3$ to the carbon supports and PtFe metals is limited. On the

188   other hand, the N is a light element and might also be surround by Pt and Fe,[26] which

189   is hard to detect under current state. In order to further investigate the structure of

190   PtFe$_3$N/C, one representative nanoparticle was investigated by high resolution

191   imaging. As seen from the HRTEM and STEM-HAADF images (Figure 2d,e), it is

192   evident that the intermetallic core structure was preserved very well after acidic

193   dealloying treatment, which means that the acidic dealloying method is efficient for

194   preparing such type of core-shell structure catalysts. The STEM-EELS images of Fe

195   and Pt are shown in Figure 2(f−h). While, it is still hard to conclude that the obtained

196   PtFe$_3$N/C nanoparticles are made of Pt-rich core-shell structures, due to the

197   overlapping images of Fe and Pt.

198   The XPS measurement was further employed to characterize the surface state of all

199   the catalysts. As shown in Figure 3(a), all the catalysts exhibit O1s peaks, and the

200   as-prepared catalysts display relatively higher intensity than Pt/C. This phenomenon

201   could be attributed to the following reasons. During the chemical leaching process, no

202   inert gas was employed to protect the oxidation of the as-prepared catalysts, which

203   would lead parts of metals being oxidized by the oxygen. Meanwhile, due to the

204   nature of the metal nanoparticles, which are easily been oxidized by oxygen in air.

205   Furthermore, for all the as-prepared catalysts, no Fe2p can be detected by XPS as

206   shown in Figure 3(b). The reason could be attributed to the acid leaching process

207   which may dissolve the Fe atoms that are near the surface of PtFe nanocrystals.[26]

208   Another reason is due to the limitation of the equipment, the XPS can only detect

209   several atomic layers from the surface, which means the majority parts of Fe are not

210   in the surface of PtFe nanocrystals after acidic dealloying. Meanwhile, as reported by

211   Wang *et al*., when annealed at high temperature, the PtFeN/C alloys could undergo

212   phase segregation in which the Pt migrates to the surface, forming a relatively pure Pt

213   overlayer on the bulk alloy, since the adsorption enthalpy of H and N on Pt is higher

214   than that on Fe.[17,26] This observation is further strengthening by the Pt4f spectra

215   shown in Figure 3(c). It can be seen from the figure that all the as-prepared catalysts

216   exhibit Pt4f characteristics, indicating that they are made of Pt-rich structures on the

217   surface.

218   Meanwhile, it was observed that, no N1s could be detected by XPS as shown in

219   Figure 3(d). The reason can be attributed to the relatively low reduction temperature,

220   which may weaken the doping effect of NH_3 to carbon supports and PtFe metals.

221   Simultaneously, due to the limitation of the equipment, the XPS can only detect

222   several atomic layers from the surface. One interesting observation is that from the

223   N1s XPS spectra as displayed in Figure 3(d), it is evident that the N1s intensity

224   increase with increasing Fe, especially in $PeFe_5N/C$, the N1s is very clear. Because all

225   the catalysts were prepared by the same method and under high-temperature post

226   treatment by NH_3 at the same temperature, the doping effect of NH_3 to carbon

227   supports and PtFe metals should be the same. Therefore, according to the results

228   obtained from XRD, STEM and XPS, it is reasonable to postulate that N does exist in

229   the as-prepared catalysts and the FeN or PtFeN as core, and there are indeed form

230   Pt-rich shell nanostructures for all the as-prepared catalysts in the present study.

231   The atomic ratios of Pt to Fe in all the as-prepared catalysts that were quantified by

232   ICP-AES are listed in Table 2. For all the as-prepared catalysts, the real atomic ratios

233   of Pt to Fe are different from the nominal ratios. This is due to the filtration step

234   during the synthesis that may inevitably lost parts of the metals and supports and

235   could affect the real ratios of Pt to Fe. While, for PtFeN/C, the real atomic ratio is

8

236 relatively lower than the nominal one, due to the ratio of Pt being relatively higher,

237 indicating that the formed core-shell structure with a relatively thicker shell could

238 efficiently prevent the dissolution of Fe. While, the real ratios for PtFe$_3$N/C and

239 PtFe$_5$N/C are relatively higher than nominal ones, due to the ratios of Pt being lower

240 than Fe, which may form a relatively thinner shell structure in both catalysts, and

241 more Fe atoms may move nearer the surface to form PtFe alloy shell, after acidic

242 dealloying, these parts of Fe could be dissolved in acid and the real Fe could decrease,

243 and consequently increase the real atomic ratios of Pt to Fe. From this perspective, the

244 shell could be easily controlled by adjust the compositions of catalysts.

245   Fig. 4(a) and (b) exhibit the CV curves of the as-prepared catalysts in N$_2$-saturated

246 0.1 mol L^{-1} HClO$_4$ aqueous solutions. By integrating the hydrogen desorption charges

247 according to the CVs in Fig. 4(a, b), the electrochemical surface area (ESA) of

248 catalysts can be calculated.[31] The ESAs of PtFeN/C, PtFe$_3$N/C, PtFe$_5$N/C and Pt/C are

249 8.72, 13.96, 10.45 and 56.48 m^2 g^{-1}. Obviously, the PtFe$_3$N/C catalysts have the

250 largest ESA compared with PtFeN/C and PtFe$_5$N/C, which might attribute to their

251 relatively lower lattice parameters and smaller crystal size. While, the ESA of

252 commercial Pt/C is 4.05 times larger than that of PtFe$_3$N/C, the reason could be

253 ascribed to the relative larger quantity of Pt in Pt/C (40 wt%), better dispersity and the

254 smaller particle size distribution.

255   The ORR curves shown in Figure 4(c) indicate that all catalysts exhibit good

256 performance for oxygen reduction, the half wave potential $E_{1/2}$ of PtFeN/C, PtFe$_3$N/C,

257 PtFe$_5$N/C and Pt/C are found to be 0.93, 0.93, 0.92 and 0.90 V *vs*. RHE, respectively,

258 indicating that the oxygen reduction process is more favorable on the as-prepared

259 catalysts than on the Pt/C. The kinetic current (I_K) can be calculated by using the

260 Koutecky–Levich equation:[32]

261
$$\frac{1}{I} = \frac{1}{I_k} + \frac{1}{I_d} \tag{3}$$

262 where I is the measured current and I_d is the diffusion limited current. The mass

263 activities (MA) for PtFeN/C, PtFe$_3$N/C, PtFe$_5$N/C and Pt/C in 0.90 V *vs*. RHE shown

264 in Fig. 4(d) are 190.24, 369.32, 315.44 and 129.15 mA mg^{-1} Pt, respectively. The

265   PtFe$_3$N/C has the highest performance for oxygen reduction, which is about 3 times

266   larger than that of the commercial Pt/C catalysts. The reason could be ascribed to the

267   acidic dealloying method which produces some pores on the PtFe crystals' surface[33]

268   and in turns increases the roughness; this roughness effect[34] also plays an important

269   role for improving the activity for oxygen reduction. Moreover, it is well known that

270   the oxygen reduction on Pt surface is mainly hindered by the relatively over strongly

271   adsorbed oxygenated intermediate species.[34,35] Tuning the *d*-band structure of Pt

272   surfaces is an effective way to weaken the adsorption of oxygenated species and thus

273   enhanced catalytic activities.[36-38] In this work, this was achieved by using iron atoms

274   in the underlying atomic layers through short-range electronic interaction with Pt or

275   through long-range geometric compressive strain effects on the Pt surface.

276   Furthermore, the lattice parameters been compressed that obtained from XRD are in

277   the sequence of PtFeN/C > PtFe$_5$N/C > PtFe$_3$N/C, which is conversed with the mass

278   activity of all the as-prepared catalysts in present work. This study directly proved

279   that the lattice parameter plays a dominant role in their high activity, this is in

280   excellent agreement with previous reports.[4] Furthemore, the NH$_3$ doping effect of

281   carbon supports could also enhance the catalytic activities for oxygen reduction as

282   widely reported, especially the pyridinic nitrogen is more favorable for oxygen

283   reduction.[29,39]

284   Furthermore, it is well known that the stability for catalysts is also significantly

285   important. Therefore, the ADT was conducted to investigate the stability of PtFe$_3$N/C

286   and Pt/C, the corresponding results are shown in Figure 5. Obviously, as showed in

287   Figure 5(a, b), the ESAs of both catalysts decreased after 30K cycles, which could be

288   associated to agglomeration, dissolution and/or detachment of the metal particles as

289   well as the corrosion of the carbon supports.[40-43] The ESA of Pt/C was found to be

290   37.04 m^2 g^{-1} after 30K cycles, which decreased 34.42%, whereas the ESA of

291   PtFe$_3$N/C was 10.82 m^2 g^{-1}, which decreased 22.49% after 30K cycles. This finding

292   indicates better stability. Figure 5(c) further presents the ORR curves of both catalysts

293   before and after ADT. Evidently, both catalysts display good stability for oxygen

294   reduction even after 30K cycles, while the change on PtFe$_3$N/C is negligible. The half

295 wave potential $E_{1/2}$ of PtFe$_3$N/C changed from 0.93 to 0.92 V after 30K accelerated

296 cycles, while, the $E_{1/2}$ for Pt/C changed from 0.90 to 0.87 V after 30K cycles.

297 Corresponding mass activities are displayed in Figure 5(d) and (e), for the PtFe$_3$N/C,

298 a decrease from 369.32 to 253.59 mA mg^{-1} Pt was observed, which decreased 31.34%,

299 while for Pt/C, decreased from 129.15 to 58.72 mA mg^{-1} Pt, which decreased 54.53%,

300 implying that the PtFe$_3$N/C is nearly two times more stable than the commercial Pt/C

301 catalysts. The reason could be ascribed to the iron nitride core, which has one of the

302 strongest covalent bonds while being very stable under normal conditions.[26] This may

303 also modify the behavior of Pt shell by inducing both geometric and electronic

304 effects.[14] Furthermore, the doping effect of NH$_3$ to the carbon supports could also

305 enhance the stability of the as-prepared catalysts by strengthening the interactions

306 between the metals and the supports as reported.[29,39]

307 **4. Conclusions**

308 In this study, a promising method has been adopted for the development of novel

309 core-shell catalysts with reduced Pt loadings while exhibiting higher ORR activity

310 and stability. The XRD, STEM, XPS and ICP were used to investigate the

311 corresponding physico-chemical characterizations of the as-prepared catalysts, which

312 exhibited Pt-rich core-shell nanostructures. Electrochemistry methods revealed that

313 the as-prepared PtFe$_3$N/C catalysts showed high ORR activity and durability due to

314 the presence of the iron nitride core that could affect the Pt shell by inducing both

315 geometric and electronic effects. Furthermore, the doping effect of NH$_3$ could also

316 enhance the interactions between the carbon supports and PtFe metals. These findings

317 further evidence the facile design and synthesis of various transition metal nitrides

318 based core-shell structures for a wide range of applications in energy conversion and

319 storage processes.

320 **Acknowledgments**

References

1   X. M. Ma, H. Meng, M. Cai and P. K. Shen, *J. Am. Chem. Soc.*, 2012, 134, 1954-1957.

2   Z. S. Li, S. Ji, B. G. Pollet and P. K. Shen, *Chem. Commun.*, 2014, 50, 566-568.

3   J. Yang, J. Yang and J. Y. Ying, *ACS Nano*, 2012, 6, 9373-9382.

4   P. Strasser, S. Koh, T. Anniyev, J. Greeley, K. More, C. F. Yu, Z. C. Liu, S. Kaya, D. Nordlund, H. Ogasawara, M. F. Toney and A. Nilsson, *Nat. Chem.*, 2010, 2, 454-460.

5   Y. G. Suo, L. Zhuang and J. T. Lu, *Angew. Chem. Int. Ed.*, 2007, 46, 2862-2864.

6   C. K. Poh, S. H. Lim, Z. Q. Tian, L. F. Lai, Y. P. Feng, Z. X. Shen and J. Y. Lin, *Nano Energy*, 2013, 2, 28-39.

7   Z. X. Yan, M. Cai and P. K. Shen, *Sci. Rep.*, 2013, 3, 1-7.

8   Z. X. Yan, G. Q. He, M. Cai, H. Meng and P. K. Shen, *J. Power Sources,* 2013, 242, 817-823.

9   Z. X. Yan, H. Meng, P. K. Shen, R. H. Wang, L. Wang, K. Y. Shi and H. G. Fu, *J. Mater. Chem.*, 2012, 22, 5072-5079.

10   S. Prabhudev, M. Bugnet, C. Bock and G. A. Botton, *ACS Nano*, 2013, 7, 6103-6110.

11   Y. C. Yu, H. L. L. Xin, R. Hovden, D. L. Wang, E. D. Rus, J. A. Mundy, D. A. Muller and H. D. Abruña, *Nano Lett.*, 2012, 12, 4417-4423.

12   V. R. Stamenkovic, B. Fowler, B. S. Mun, G. Wang, P. N. Ross, C. A. Lucas and N. M. Marković, *Science*, 2007, 315, 493-497.

13   X. Huang, E. Zhu, Y. Chen, Y. Li, C.Y. Chiu, Y. Xu, Z. Lin, X. Duan and Y. Huang, *Adv. Mater.*, 2013, 25, 2974-2979.

14   L. Gan, M. Heggen, S. Rudi and P. Strasser, *Nano Lett.*, 2012, 12, 5423-5430.

15   S. B. Yin, M. Cai, C. X. Wang and P. K. Shen, *Energy Environ. Sci.*, 2011, 4, 558-563.

16   S. C. Mu, P. Zhao, C. Xu, Y. Gao and M. Pan, *Int. J. Hydrogen Energy,* 2010, 35, 8155-8160.

352 17 D. L. Wang, H. L. Xin, Y. C. Yu, H. S. Wang, E. Rus, D. A. Muller and H. D.
353   Abruña, *J. Am. Chem. Soc.*, 2010, 132, 17664-17666.

354 18 D. L. Wang, H. L. Xin, H. S. Wang, Y. C. Yu, E. Rus, D. A. Muller, F. J. DiSalvo
355   and H. D. Abruña, *Chem. Mater.*, 2012, 24, 2274-2281.

356 19 J. Durst, M. Lopez-Haro, L. Dubau, M. Chatenet, Y. Soldo-Olivier, L. Guétaz, P.
357   Bayle-Guillemaud and F. Maillard, *J. Phys. Chem. Lett.*, 2014, 5, 434-439.

358 20 K. A. Kuttiyiel, K. Sasaki, Y. Choi, D. Su, P. Liu and R. R. Adzic, *Energy
359   Environ. Sci.*, 2012, 5, 5297-5304.

360 21 D. L. Wang, Y. C. Yu, H. L. Xin, R. Hovden, P. Ercius, J. A. Mundy, H. Chen, J.
361   H. Richard, D. A. Muller, F. J. DiSalvo and H. D. Abruña, *Nano Lett.*, 2012, 12,
362   5230-5238.

363 22 B. N. Wanjala, J. Luo, R. Loukrakpam, B. Fang, D. Mott, P. N. Njoki, M.
364   Engelhard, H. R. Naslund, J. K. Wu, L. Wang, O. Malis and C. J. Zhong, *Chem.
365   Mater.*, 2010, 22, 4282-4294.

366 23 V. Mazumder, M. F. Chi, K. L. More and S. H. Sun, *J. Am. Chem. Soc.*, 2010,
367   132, 7848–7849.

368 24 A. Morozan, B. Jousselme and S. Palacin, *Energy Environ. Sci.*, 2011, 4,
369   1238-1254.

370 25 H. Yang, *Angew. Chem. Int. Ed.*, 2011, 50, 2674-2676.

371 26 K. A. Kuttiyiel, K. Sasaki, Y. M. Choi, D. Su, P. Liu and R. R. Adzic, *Nano Lett.*,
372   2012, 12, 6266-6271.

373 27 C. Wang, M. F. Chi, G. F. Wang, D. van der Vliet, D. G. Li, K. More, H. H. Wang,
374   J. A. Schlueter, N. M. Markovic and V. R. Stamenkovic, *Adv. Funct. Mater.*, 2011,
375   21, 147-152.

376 28 Q. Y. Lu, B. Yang, L. Zhuang and J. T. Lu, *J. Phys. Chem. B,* 2005, 109,
377   8873-8879.

378 29 S. Y. Jing, L. Luo, S. B. Yin, F. Huang, Y. Jia, Y. Wei, Z. H. Sun and Y. M. Zhao,
379   *Appl. Catal. B*, 2014, 147, 897-903.

380 30 Y. Garsany, J. J. Ge, J. St-Pierre, R. Rocheleau and K. E. Swider-Lyons, *J
381   Electrochem. Soc.*, 2014, 161, F628-F640.

382 31 S. B. Yin, P. K. Shen, S. Q. Song and S. P. Jiang, *Electrochim. Acta,* 2009, 54,
383   6954-6958.

384 32 D. L. Wang, H. L. L. Xin, R. Hovden, H. S. Wang, Y. C. Yu, D. A. Muller, F. J.
385   DiSalvo and H. D. Abruña, *Nat. Mater.*, 2013, 12, 81-87.

386 34 Y. Cai, C. Ma, Y. M. Zhu, J. X. Wang and R. R. Adzic, *Langmuir*, 2011, 27,
387   8540-8547.

388 35 S. W. Lee, S. Chen, J. Suntivich, K. Sasaki, R. R. Adzic and Y. Shao-Horn, *J.*
389   *Phys. Chem. Lett.*, 2010, 1, 1316-1320.

390 36 V. Stamenkovic, B. S. Mun, K. J. J. Mayrhofer, P. N. Ross, N. M. Markovic, J.
391   Rossmeisl, J. Greeley and J. K. Norskov, *Angew. Chem. Int. Ed.*, 2006, 45,
392   2897-2901.

393 37 V. R. Stamenkovic, B. S. Mun, K. J. J. Mayrhofer, P. N. Ross and N. M.
394   Markovic, *J. Am. Chem. Soc.*, 2006, 128, 8813-8819.

395 38 J. Greeley, I. E. L. Stephens, A. S. Bondarenko, T. P. Johansson, H. A. Hansen, T.
396   F. Jaramillo, J. Rossmeisl, I. Chorkendorff and J. K. Norskov, *Nat. Chem.*, 2009,
397   1, 552-556.

398 39 S. Kundu, T. C. Nagaiah, W. Xia, Y. Wang, S. V. Dommele, J. H. Bitter, M. Santa,
399   G. Grundmeier, M. Bron, W. Schuhmann and M. Muhler, *J Phys. Chem. C*, 2009,
400   113, 14302–14310.

401 40 Z. X. Yan, J. M. Xie, J. J. Jing, M. M. Zhang, W. Wei and S. B. Yin, *Int. J.*
402   *Hydrogen Energy,* 2012, 37, 15948-15955.

403 41 Z. X. Yan, W. Wei, J. M. Xie, S. C. Meng, X. Lu and J. J. Zhu, *J. Power Sources,*
404   2013, 222, 218-224.

405 42 S. B. Yin, S. C. Mu, H. F. Lv, N. C. Cheng, M. Pan and Z. Y. Fu, *Appl. Catal. B*,
406   2010, 93, 233-240.

407 43 S. B. Yin, S. C. Mu, M. Pan and Z. Y. Fu, *J. Power Sources,* 2011, 196,
408   7931-7936.

409

410   **Figure captions**

411   **Figure 1.** (a) XRD curves of the as-prepared samples with a scan rate of 5° min^{-1}. (b)

412   Curve fitting for (111) diffraction peaks in part (a).

413   **Figure 2.** (a, b) BF and ADF-STEM overview images of PtFe$_3$N/C intermetallic

414   nanoparticles after acidic dealloying, (c) EDX mapping of PtFe$_3$N/C, (d, e) HRTEM

415   and STEM-HAADF images of PtFe$_3$N/C after acidic dealloying, (f) EELS mapping of

416   Fe L$_{2,3}$ edge, (g) EELS mapping of Pt N$_3$ edge and (h) combination of (f) and (g). The

417   bars in (e) to (h) are indicating a length of 5 nm.

418   **Figure 3.** XPS surveys for the as-prepared catalysts (a), Fe2p (b), Pt4f (c) and N1s

419   (d).

420   **Figure 4.** (a, b) The CV curves for the as-prepared catalysts in N$_2$-purged 0.1 mol L^{-1}

421   HClO$_4$ aqueous solutions at 25 $^{\circ}$C, scan rate 50 mV s^{-1}, (c) ORR polarization curves

422   for the catalysts in O$_2$-saturated 0.1 mol L^{-1} HClO$_4$ aqueous solutions at 25 $^{\circ}$C, scan

423   rate 5 mV s^{-1}, rotating rate 1600 rpm, the insert is the zoom of the polarization area of

424   (c). (d) Comparison of mass activities (MA): (1) PtFeN/C, (2) PtFe$_3$N/C, (3) PtFe$_5$N/C

425   and (4) Pt/C.

426   **Figure 5.** CVs for (a) PtFe$_3$N/C and (b) Pt/C catalysts in N$_2$-purged 0.1 mol L^{-1}

427   HClO$_4$ aqueous solutions before and after ADT, 25 $^{\circ}$C, scan rate 50 mV s^{-1}. (c) ORR

428   polarization curves for PtFe$_3$N/C and Pt/C catalysts in O$_2$-saturated 0.1 mol L^{-1}

429   HClO$_4$ aqueous solutions before and after ADT, 25 $^{\circ}$C, scan rate 5 mV s^{-1}, rotating

430   rate 1600 rpm. (d) Comparison of mass activities (MA) before and after cycling. (e)

431   Comparison of mass activities for PtFe$_3$N/C and Pt/C before and after cycling at 0.90

432   V and 0.85 V.

433   **Table 1** Structural parameters of the samples extracted from X-ray powder diffraction.

434   **Table 2** Contents and atomic ratios of Pt to Fe in all the investigated catalysts.

435   **Table 3** Summary of electrochemical surface area (S_{ESA}), half wave potential ($E_{1/2}$),

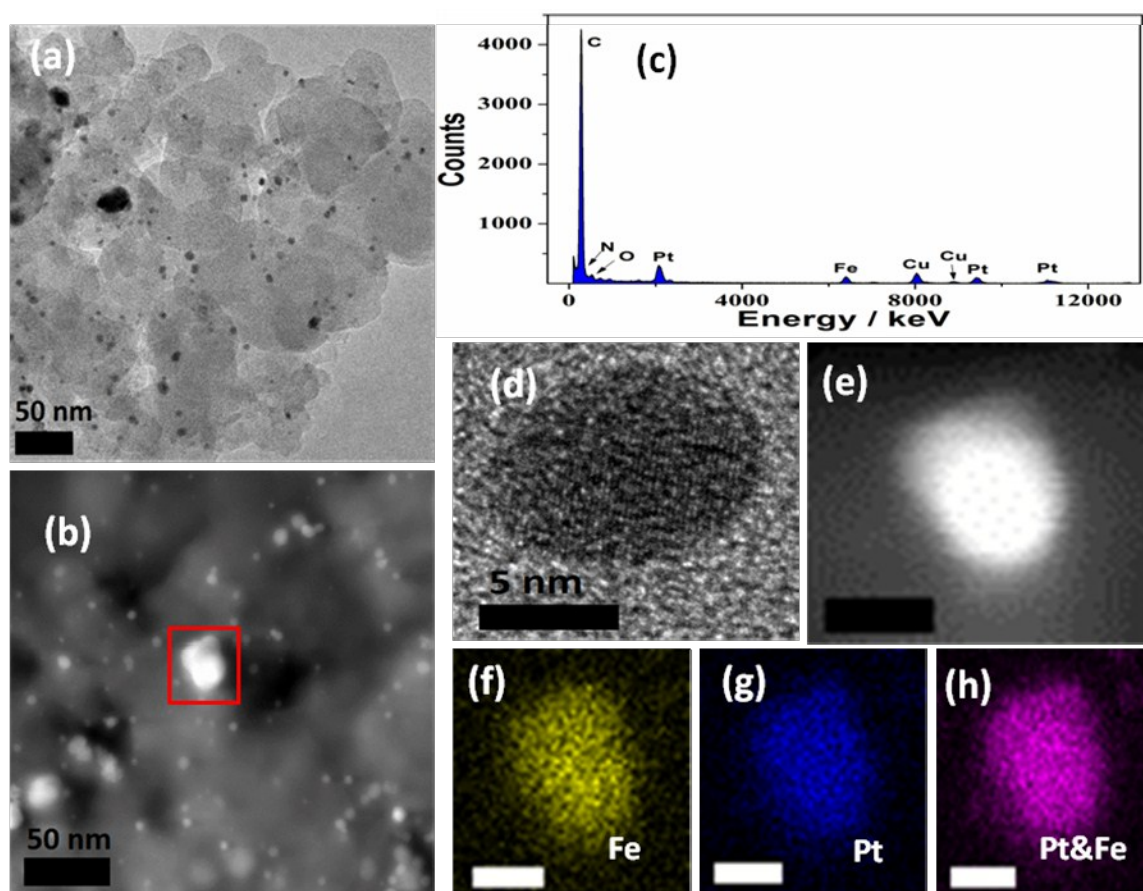436   and mass activity (MA) of ORR at 0.9 V vs. RHE.
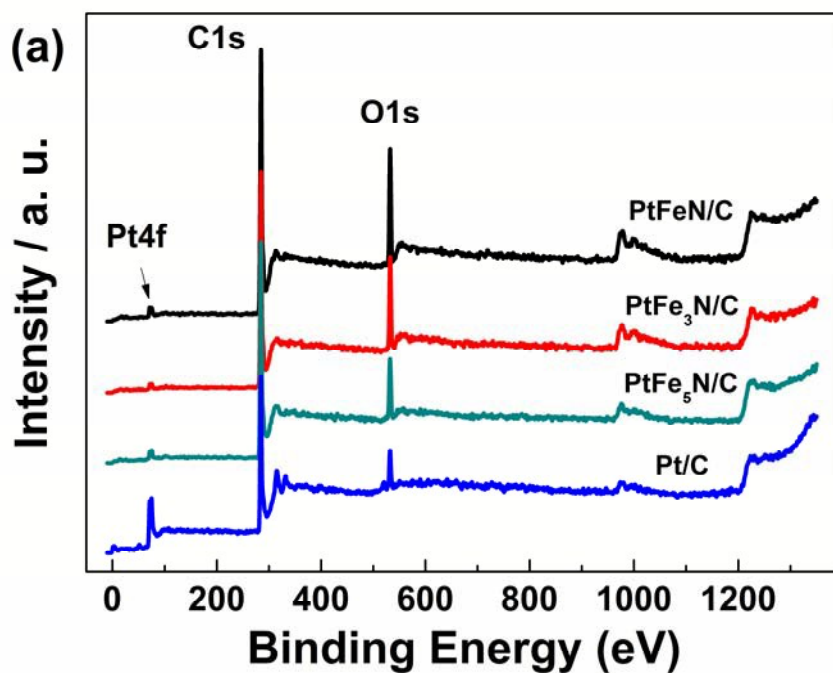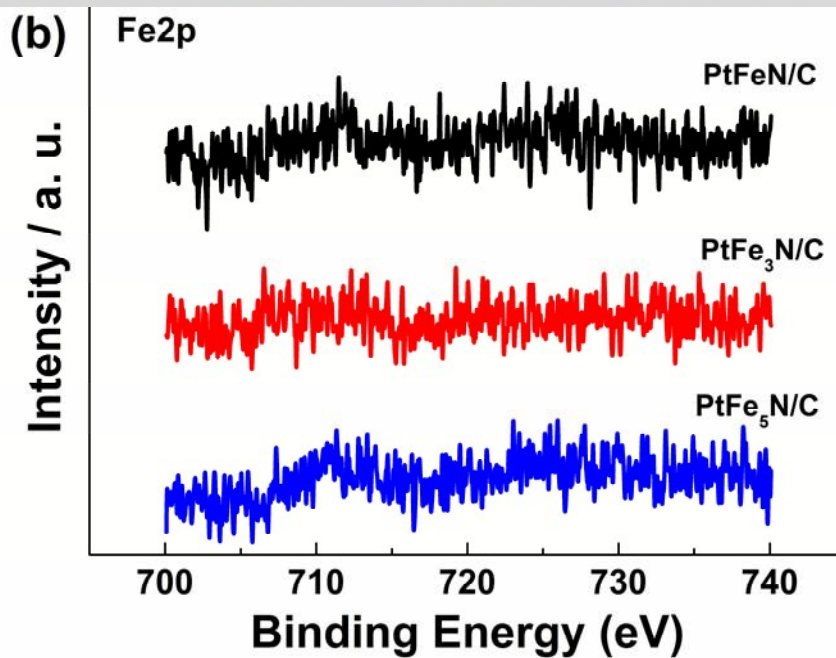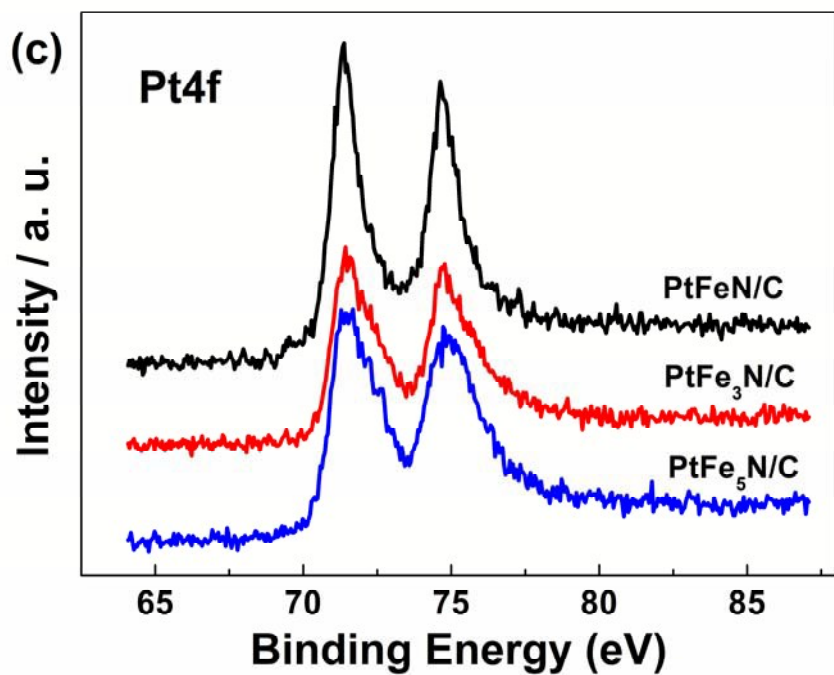
437

438 **Figure 1.**
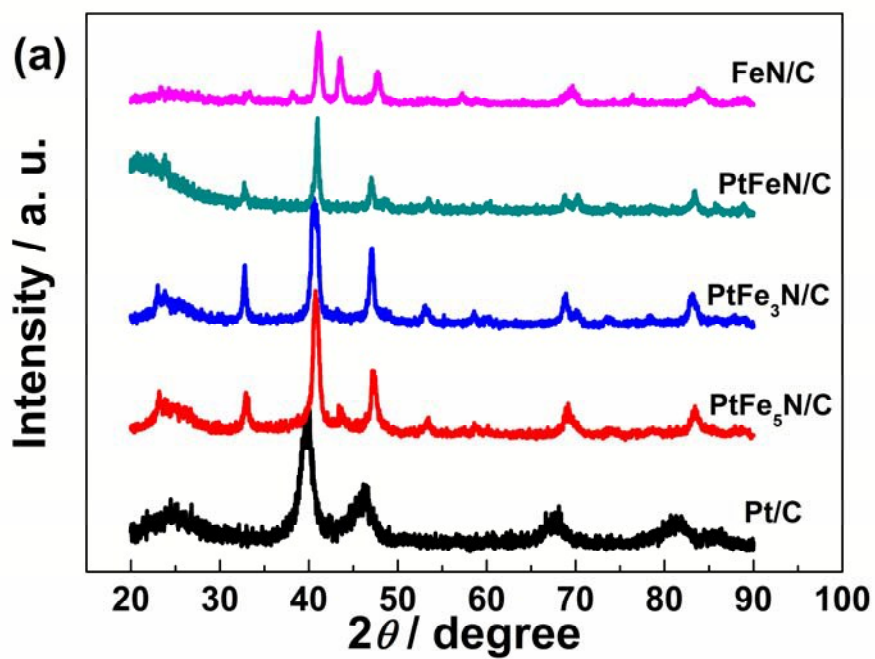
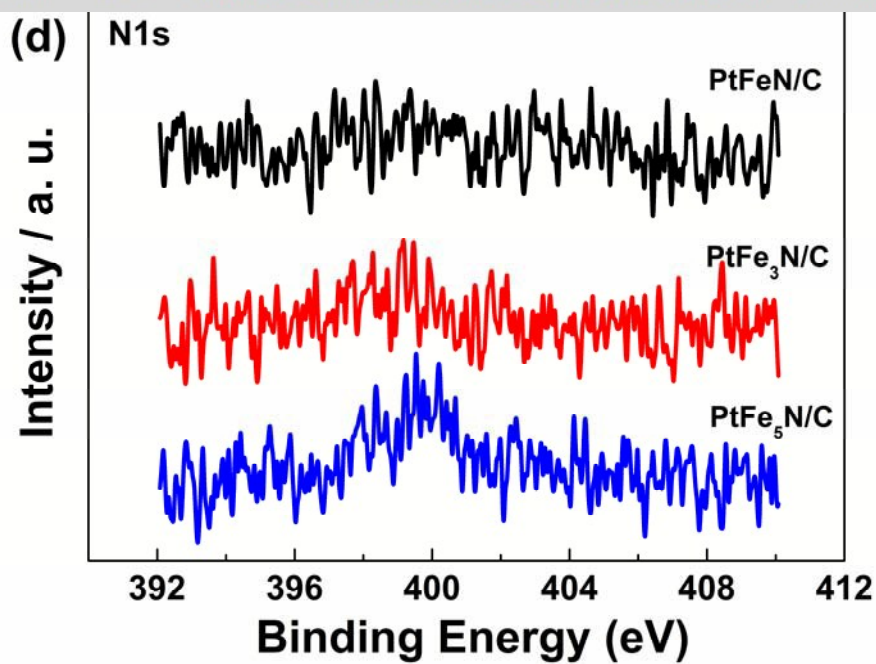

439
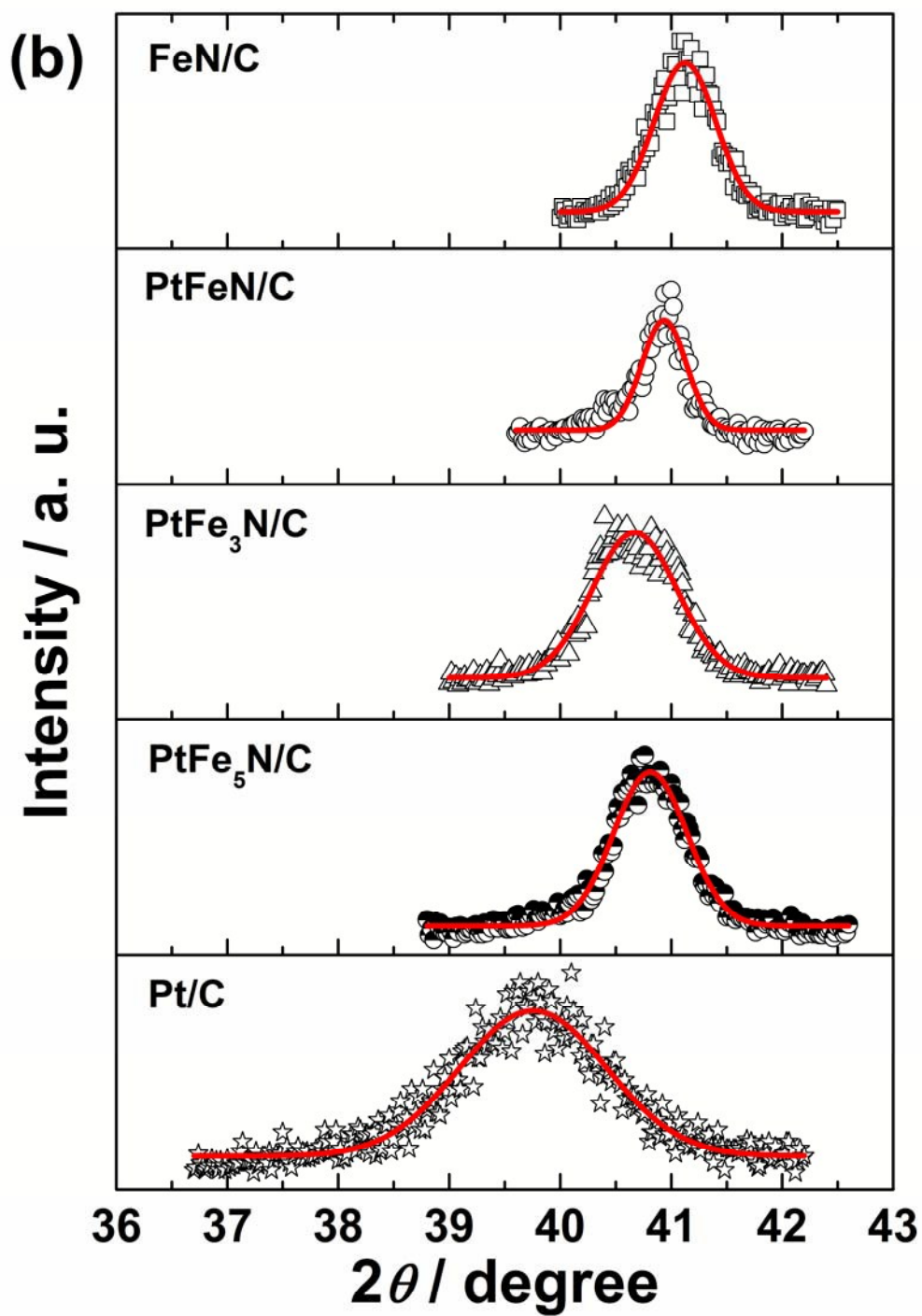
440
441
442

443 **Figure 2.**
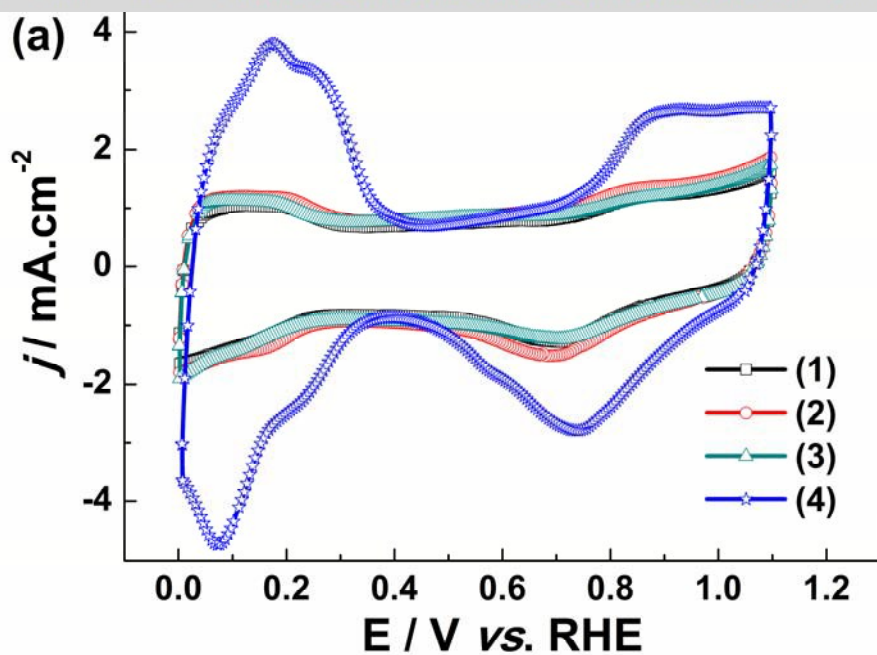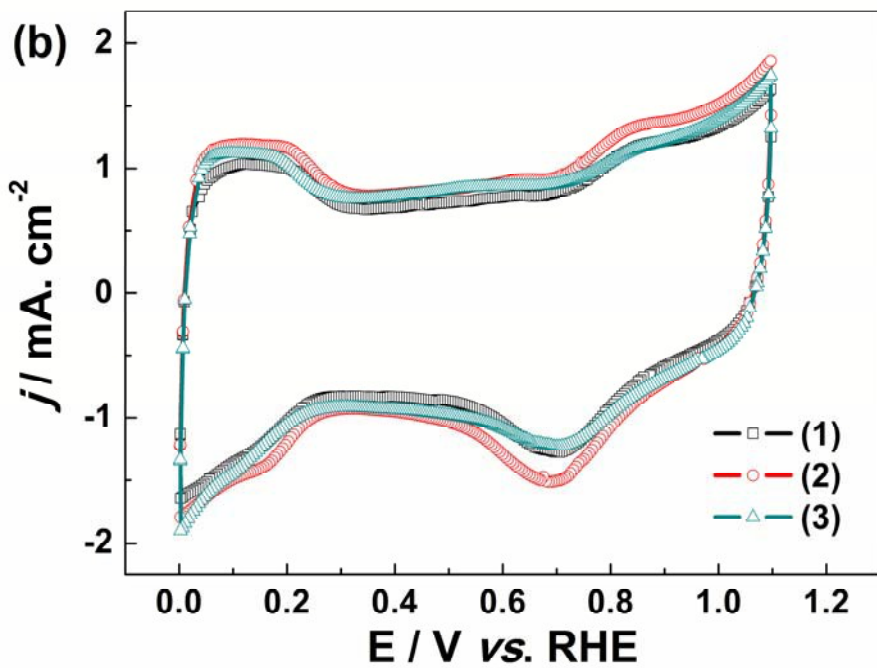

444

445

446

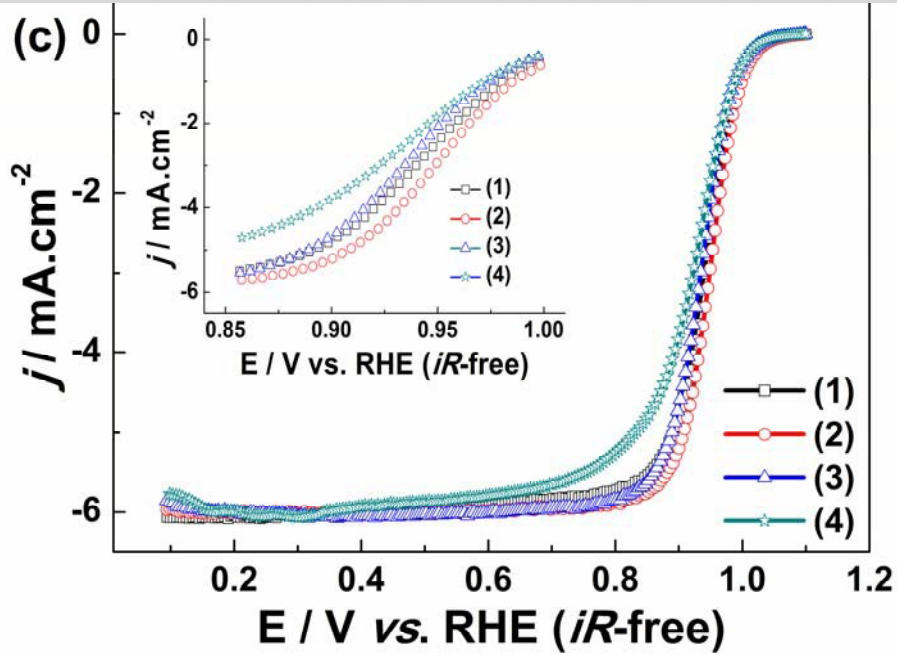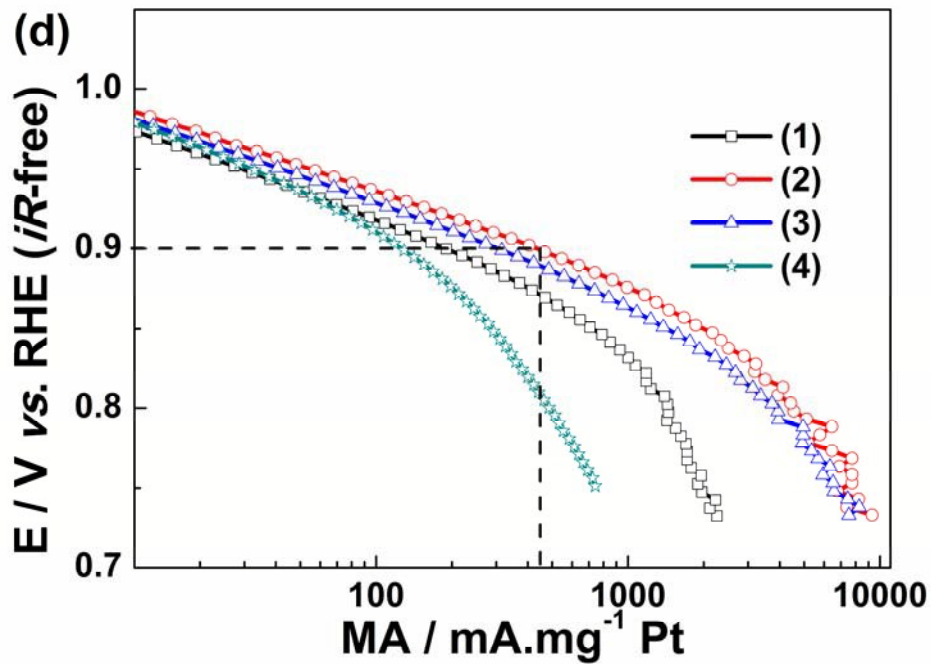447   **Figure 3.**

448

449

450

451

452

453

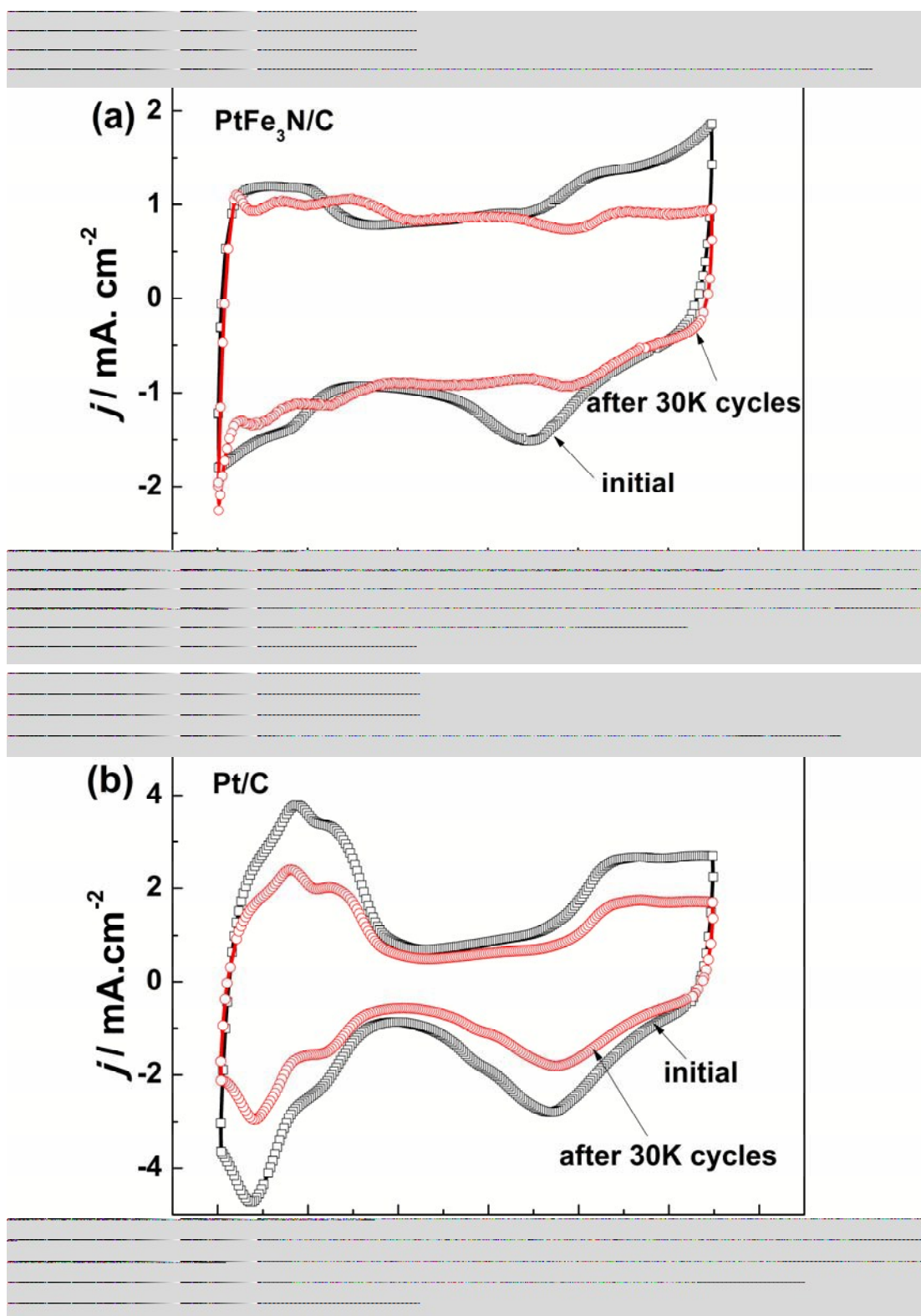454   **Figure 4.**

455

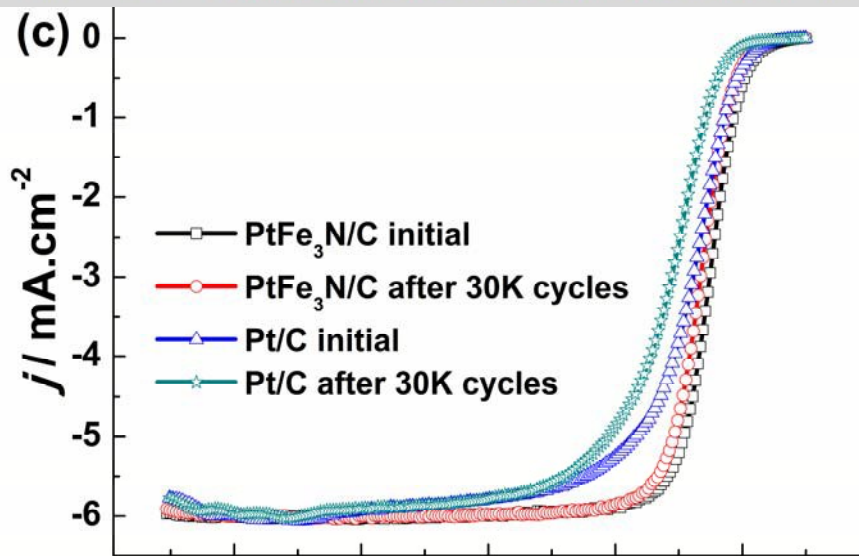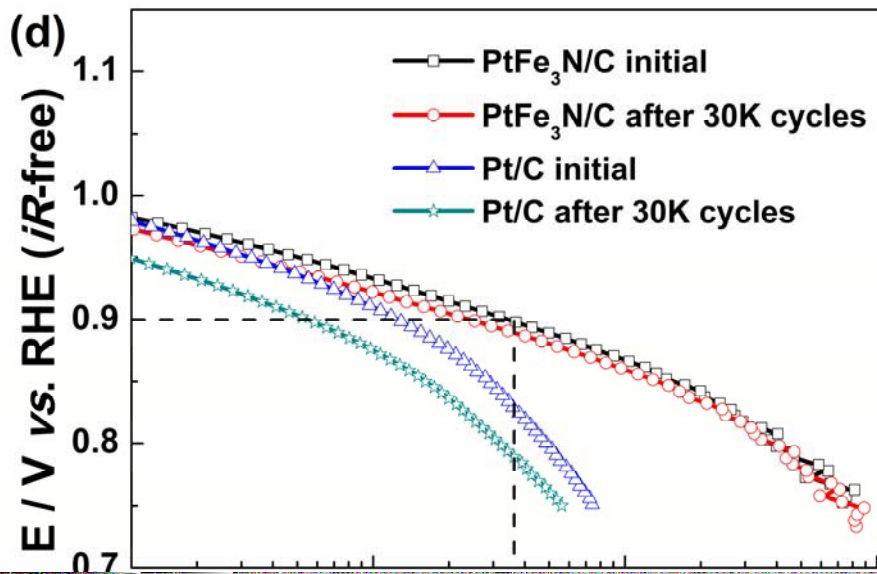456

457

458

459

460

461   **Figure 5.**
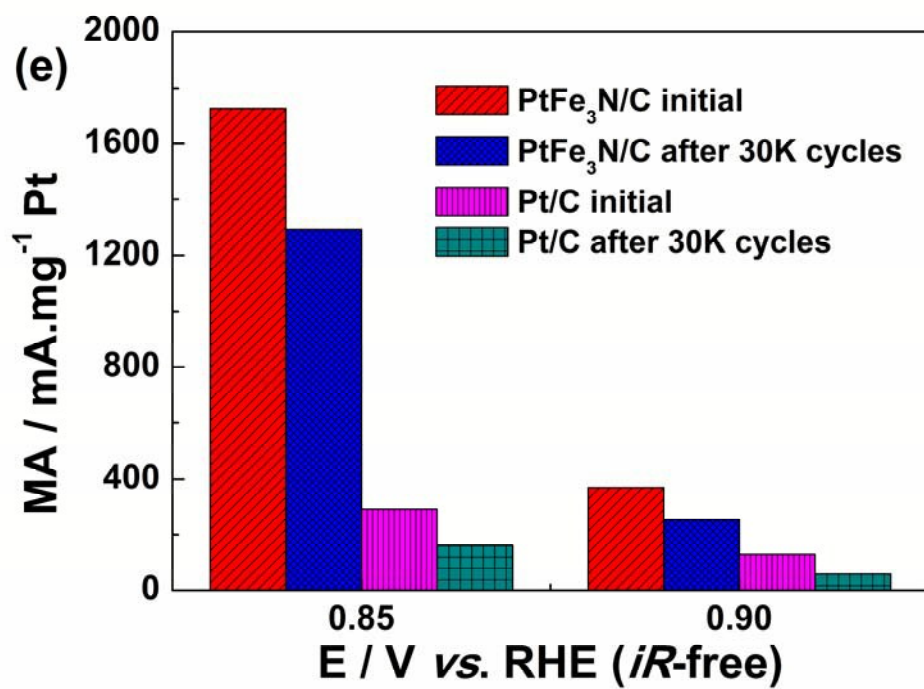

462

463

464

465

(e)

466
467

468 **Table 1**

469

Name	2θ (degree) (111) facet	Lattice parameter (Å) α	Crystal size (nm)
FeN/C	41.12	6.2063	12.51
PtFeN/C	40.93	6.2336	14.73
PtFe$_3$N/C	40.67	6.2725	9.72
PtFe$_5$N/C	40.81	6.2517	10.13
Pt/C	39.76	6.4106	2.71

470

471

472 **Table 2**

473

Name	η_{Pt}/wt% (nominal)	η_{Fe}/wt% (nominal)	Pt:Fe atoimc ratios (nominal)	η_{Pt}/wt% (real)	η_{Fe}/wt% (real)	Pt:Fe atomic ratios (real)
PtFeN/C	15.68	4.33	1.0	15.03	5.61	0.77
PtFe₃N/C	10.82	9.08	0.57	11.42	5.47	0.60
PtFe₅N/C	8.33	11.67	0.30	11.9	7.85	0.43
Pt/C	40.00	—	—	40.00	—	—

474

475

476   **Table 3**

477

Name	S_{ESA} (m^2 g^{-1}) initial	S_{ESA} (m^2 g^{-1}) after 30k cycles	$E_{1/2}$ (V) initial	$E_{1/2}$ (V) after 30k cycles	MA (mA mg^{-1} Pt) initial	MA (mA mg^{-1} Pt) after 30k cycles
PtFeN/C	8.72	—	0.93	—	190.24	—
PtFe$_3$N/C	13.96	10.82	0.93	0.92	369.32	253.59
PtFe$_5$N/C	10.45	—	0.92	—	315.44	—
Pt/C	56.48	37.04	0.90	0.87	129.15	58.72

478

Graphical Abstract
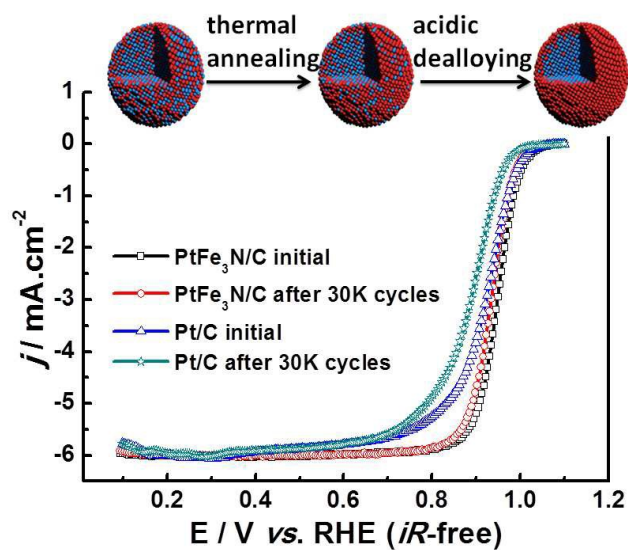
The PtFe$_3$N/C has good activity for ORR, which also has amazing stability even after 30k cycles accelerated durability test.